buildings

MDPI

Article

A Stress Measurement Method for Steel Strands Based on Spatially Self-Magnetic Flux Leakage Field

Shangkai Liu [1], Cheng Cheng [2], Ruiqiang Zhao [3,*], Jianting Zhou [1] and Kai Tong [1]

[1] State Key Laboratory of Mountain Bridge and Tunnel Engineering, Chongqing Jiaotong University, Chongqing 400074, China; skliu@mails.cqjtu.edu.cn (S.L.); jtzhou@cqjtu.edu.cn (J.Z.); kaitong@mails.cqjtu.edu.cn (K.T.)
[2] Chongqing Wukang Technology Co., Ltd., Chongqing 404000, China; chengcheng@cmhk.com
[3] School of Materials Science and Engineering, Chongqing Jiaotong University, Chongqing 400074, China
* Correspondence: rqzhao@cqjtu.edu.cn; Tel.: +86-153-2036-4035

Abstract: Metal Magnetic Memory (MMM) exhibits the advantage of not requiring embedded sensors or external excitation, making it suitable for inspecting ferromagnetic components in engineering structures. This study introduced MMM into stress detection of steel strands. Graded tensile tests were conducted on the steel strands to investigate the correlation between Self-Magnetic Flux Leakage (SMFL) signals and stress levels. Different spatial detection positions with varying Lift-Off Values (LOV) and Rotation Angle Values (RAV) were set to examine the distribution of spatial SMFL field under load. Furthermore, a magnetic characteristic parameter A_N was proposed to assess the stress level of the steel strands. The results indicate that the rate of change in the middle region of the SMFL curve was lower than that at the beginning and the end. Additionally, with increased applied load, the SMFL curve exhibited systematic variations, and the dispersion of the normal component curve gradually decreased. By utilizing the magnetic characteristic parameter A_N, the stress in the steel strands can be calculated, with the parameters determined based on LOV and RAV. This achievement expanded the nondestructive testing methods for steel strands and holds significant research value.

Keywords: steel strand; stress detection; metal magnetic memory; spatially SMFL field; detection position

Citation: Liu, S.; Cheng, C.; Zhao, R.; Zhou, J.; Tong, K. A Stress Measurement Method for Steel Strands Based on Spatially Self-Magnetic Flux Leakage Field. *Buildings* **2023**, *13*, 2312. https://doi.org/10.3390/buildings13092312

Academic Editor: Huiyong Ban

Received: 2 August 2023
Revised: 11 September 2023
Accepted: 11 September 2023
Published: 12 September 2023

1. Introduction

Steel strands are commonly used in critical load-bearing components of bridges, such as inclined cables, suspender rods, and main cables. Accurately understanding the stress state of steel strands can effectively ensure the safe operation of bridges [1,2].

Nondestructive testing is the basis of structural health monitoring and can improve the efficiency of structural reinforcement [3,4]. Common nondestructive testing methods for tension include: (i) the fiber Bragg grating-based method [5], which measures the strain of steel strands using the principle of fiber Bragg gratings, offering advantages of high-speed detection, high precision, and strong anti-interference capability, but with the drawback of high cost and complex installation and usage; (ii) the vibration frequency method [6], which detects tension based on the relationship between the natural frequency of steel strands and their stress state, providing advantages of rapid and efficient testing with good repeatability, but susceptible to environmental influences, limited applicability, and requiring specialized equipment; (iii) the magnetic flux method [7], which indirectly infers the stress state of steel strands by measuring the changes in magnetic flux, offering the advantages of high sensitivity and quantitative detection, but also affected by environmental factors and requiring complex equipment and specialized operation.

The common issue with the above methods is the need for embedded sensors or external excitation, marking the installation and application of the testing equipment relatively complex [8]. Metal Magnetic Memory (MMM) detection is an environmentally

friendly, non-exciting, nondestructive testing method. It features lightweight detection instruments and does not require embedded sensors, making it of significant engineering significance when applied to the stress detection of steel strands [9,10].

The foundation of MMM detection lies in the Self-Magnetic Flux Leakage (SMFL) effect [11], which refers to local magnetic field changes inside magnetic materials without an external magnetic field due to defects or stress concentrations [12–14]. MMM detection determines defects in structures by measuring the SMFL field changes of ferromagnetic materials, and it is suitable for detecting microscopic defects [15,16], making it widely applied in fields such as pipeline transportation, power facilities, and industrial manufacturing [17–19].

Meanwhile, scholars have conducted extensive research on this technology, proposing magneto-mechanical models [20], energy conservation laws [21], magnetic dipole models [22], and other theories. They have also conducted experiments on various components, including reinforcing bars [23], steel structures [24,25], and welds [26]. Numerous studies have been conducted in terms of evaluation indicators for MMM detection. Roskosz measured the Residual Magnetic Field (RMF) signal on the surface of specimens under load and found that the tangential component parallel to the direction of the load is most correlated with the stress level [27], proposing a residual stress evaluation method based on RMF gradient [28]. Zhou measured the Self-Magnetic Flux Leakage (SMFL) signal of corroded reinforced concrete and found that the normal component $H_S(Z)$ of the SMFL signal can qualitatively determine the location and degree of reinforcement corrosion. The $H_S(Z)$ gradient is approximately linearly correlated with the flexural strength loss rate of the beam [29]. Huang proposed using the maximum gradient K_{max} of the normal component $H_p(y)$ of the magnetic model to represent the degree of stress concentration [30]. Yao proposed using the peak-to-peak amplitude of the normal and tangential gradient curves of local magnetic signals, along with horizontal distances $W(X)_{p\text{-}p}$, $W(Y)_{p\text{-}p}$, $S(X)_{p\text{-}p}$, and $S(Y)_{p\text{-}p}$, to characterize the degree and scope of plastic deformation [31].

To sum up, research on metal magnetic memory has mainly focused on the microscopic damage, stress state, and stress concentration detection in ferromagnetic materials [12,32]. Stress detection was primarily conducted on standard specimens and reinforcing bars with distinct elastic and plastic stages [33–36]. However, in the case of steel strands, this technology was mainly utilized for detecting corrosion damage, and there is limited research on stress detection in steel strands and the impact of spatial detection positions on the results [37,38].

Therefore, this experiment subjected steel strands to graded loading to investigate the SMFL field distribution under different load conditions. A stress measurement method for steel strands based on the spontaneous SMFL field is proposed. The influence of LOV (the vertical distance between the sensor surface and the tested specimen) and RAV (the clockwise rotation angle of the sensor with the initial position as the origin and the tested specimen as the center) on the detection results was discussed.

This study presents a method to measure the working stress of steel strands using the magnetic characteristic parameters A_N (normalized mean absolute deviation). Section 1 introduces the basic principles and research status of Metal Magnetic Memory (MMM) detection and its application to stress detection in steel strands. Section 2 describes the theoretical derivation of the relationship between SMFL signals and stress using the Jiles–Atherton model. Section 3 presented the experimental design for collecting SMFL signals. Section 4 analyzes the distribution of the original magnetic field and SMFL field on the surface of the specimens under graded loading. Section 5 discusses the relationship between the normal component of the SMFL field and applied loads for different sampling points or spatial detection positions. The study proposes a calculation method for steel strand stress based on the magnetic characteristic parameter A_N and further investigates the effects of LOV and RAV on the detection results.

2. Theoretical Background

2.1. Effect of Applied Stress on Magnetic Properties of Materials

In MMM detection, components exhibit the phenomenon of maximum tangential component and zero-crossing point of the normal component of the SMFL field in the damaged or stress-concentrated areas. However, research on the magnetic domain is required for components with magnetic field redistribution caused by axial tension, where the stress-concentrated area is not clearly defined.

A magnetic domain refers to regions in ferromagnetic materials with the same magnetization direction at the microscopic scale. Without an external magnetic field, magnetic domains in ferromagnetic materials are randomly distributed. The applied stress is equivalent to applying an external magnetic field to the magnetic domains, resulting in a directional distribution of the magnetic domains and altering the material's magnetism, ultimately manifesting as an additional magnetic field on the material's surface, as shown in Figure 1.

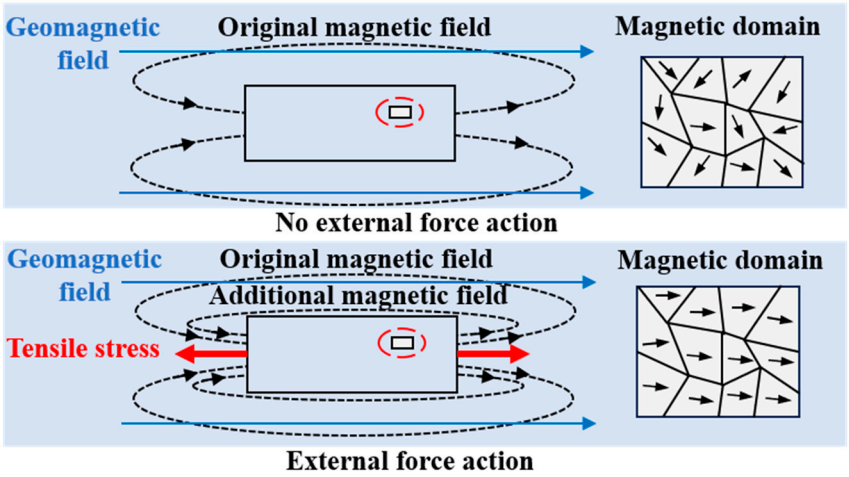

Figure 1. Magnetic field distribution and internal magnetic domain changes of components under external stress.

2.2. Jiles–Atherton Model

To further analyze the influence of stress on the distribution of the leakage magnetic field and explore the magneto-mechanical coupling mechanism, it is necessary to apply the Jiles–Atherton (J-A) model [39,40]. The J-A model was derived from Jiles and Atherton's theory of ferromagnetization. These scholars pointed out that uniaxial stress can change the internal effective field through magnetostriction. Under an external magnetic field, the magnetization of a ferromagnetic material was composed of reversible magnetization caused by domain wall bending and reversible magnetization caused by domain wall movement.

The impact of applied stress on magnetization is equivalent to adding a magnetic field H_σ to the magnetic domain structure. This additional field is described by the energy A along the reversible non-hysteresis magnetization curve [41,42].

$$A = \mu_0 HM + \frac{H_0}{2}\alpha M^2 + \frac{3}{2}\alpha\lambda + TS \tag{1}$$

where T is temperature, S is entropy, H is the external magnetic field, M is the magnetization intensity, α is the domain coupling coefficient, σ is the applied stress, and λ is the magnetostriction coefficient.

The effective field H_e can be expressed as the derivative of energy A concerning magnetization intensity M.

$$H_e = \frac{1}{M_0}\frac{dA}{dM} = H + \alpha M + \frac{3}{2}\frac{\sigma}{\mu_0}\frac{d\lambda}{dM} \tag{2}$$

when the applied stress σ_0 is not in the same direction as λ and M, the stress used in Equation (2) represents the component of stress applied along that direction. For isotropic materials:

$$\sigma = \sigma_0\left(\cos^2\theta - v\sin^2\theta\right) \tag{3}$$

where θ is the angle between the applied stress σ_0 and the direction of the magnetic field strength H, and V is the Poisson's ratio. The effective field component H_σ caused by the applied stress is calculated as follows:

$$H_\sigma = \frac{3}{2}\frac{\sigma}{\mu_0}\left(\frac{d\lambda}{dM}\right)_\sigma = \frac{3}{2}\frac{\sigma_0}{\mu_0}\left(\frac{d\lambda}{dM}\right)_\sigma\left(\cos^2\theta - v\sin^2\theta\right) \tag{4}$$

Before calculating H_σ, it is necessary to determine the magnetostriction coefficient λ of the material, which is related to the magnetization intensity M [39]:

$$\lambda = \sum_{i=0}^{\infty}\gamma_i M^{2i} \tag{5}$$

when calculating the magnetostriction coefficient of ferromagnetic materials, i = 2 is more reasonable:

$$\lambda = \gamma_1 M^2 + \gamma_2 M^4 \tag{6}$$

The relationship between the magnetostriction coefficient and stress is represented using a Taylor series expansion:

$$\gamma_i(\sigma) = \gamma_i(0) + \sum_{n=1}^{\infty}\frac{\sigma^n}{n!}\gamma_i^n(0) \tag{7}$$

where $\gamma_i(\sigma)$ represents the nth-order derivative γ_i corresponding to σ = 0. For ferromagnetic materials, n = 1, and $\gamma_i(\sigma)$ is substituted into Equations (2) and (4):

$$H_\sigma = \frac{3\sigma}{2H_0}\left[\left(2\gamma_1(0) + 2\gamma'_1(0)\sigma\right)M + \left(4\gamma_2(0) + 4\gamma'_2(0)\sigma\right)\right]M^3 \tag{8}$$

$$H_e = H + \alpha M + \frac{3\sigma}{2H_0}\left[\left(2\gamma_1(0) + 2\gamma'_1(0)\sigma\right)M + \left(4\gamma_2(0) + 4\gamma'_2(0)\sigma\right)\right]M^3 \tag{9}$$

From this, it can be observed that if $H_\sigma > 0$, the application of stress strengthens the existing magnetic field, while if $H_\sigma < 0$, the effect of stress weakens the existing magnetic field. The application of stress significantly influences the distribution of the existing magnetic field, and this effect shows non-linear changes with increasing stress.

3. Experimental Material and Methods

To explore the stress detection method based on the SMFL effect, this study conducted experiments on 1860-grade steel strands using a universal testing machine to clarify the surface leakage magnetic field distribution of steel strands under different stress states. The steel strands were subjected to uniform tension at a constant speed and maintained at the design tension value. The sensor was scanned along the axial direction of the specimen at the designated positions.

3.1. Experimental Specimen and Platform

The steel strand used in this experiment was of type Φs15.24(1×7), with a nominal diameter of 15.2 mm, composed of 7 steel wires, each having a diameter of 5 mm. The material parameters are shown in Table 1.

Table 1. Chemical composition and mechanical properties of steel strand test piece.

Chemical Composition/%					Mechanical Properties			
C	Si	Mn	S	P	Tensile Strength/MPa	Modulus of Elasticity/GPa	Hardness	Coefficient of Friction
0.75~0.85	0.12~0.32	0.60~0.90	<0.025	<0.025	1860	193.9	HRC 40~45	0.15~0.25

The steel strands were transformed into test specimens of 80 cm in length. Before testing, the PE protective sheath and anticorrosive grease were removed from the surface. The specimens were clamped and stretched using the universal testing machine, with a 15 cm clamping length on both sides. Aluminum Anti-skid Spacers were inserted in the clamping area to prevent slippage between the specimen and the fixture.

In practical engineering scenarios, pre-magnetizing steel specimens is often not feasible. Therefore, a single steel wire was cut into multiple segments for testing in this experiment, and no pre-magnetization was applied to the specimens. Additionally, no external magnetic field source was introduced. Consequently, the initial magnetization strength of the specimens falls between demagnetized and saturated magnetization. This approach closely simulates the real-world usage conditions of steel strands, laying a solid foundation for the practical application of this technology.

The relationship between initial magnetization strength and initial magnetic field strength is as follows:

$$M_i = \mu_0 H_i(\mu_r - 1) \tag{10}$$

where μ_r represents the relative magnetic permeability, μ_0 represents the vacuum magnetic permeability, taken as $4\pi \times 10^{-7}$ N/A^2, M_i represents the initial magnetization strength, and H_i represents the initial magnetic field strength.

The HMR2300 magnetic probe with an accuracy of 70 microgauss was utilized to collect the SMFL signals. The data were transmitted via a serial port server and stored on a computer, as depicted in Figure 2. A coordinate system was established with the magnetic probe as the origin. The relative position between the probe and the specimen determined that: (i) the y-axis was parallel to the specimen axis, (ii) the z-axis was perpendicular to the specimen axis, and (iii) the x-axis was perpendicular to the y–z plane.

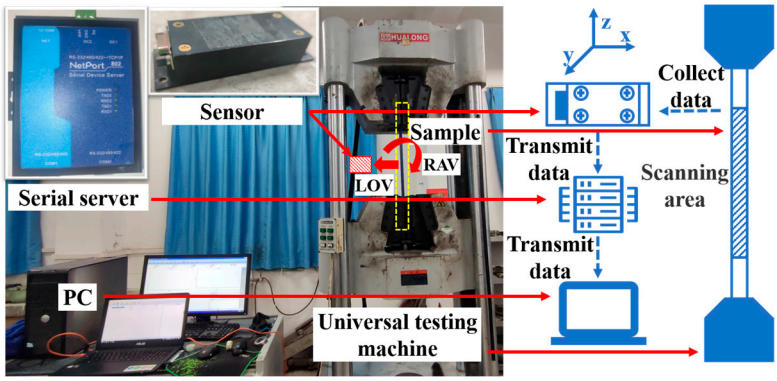

Figure 2. Schematic diagram of the experimental platform.

The position of the sensor is determined by the scanning area, lift-off value (LOV), and Rotation Angle Values (RAV). The scanning area is parallel to the test piece, indicating the moving range of the sensor during one scan. LOV is the vertical distance between the sensor surface and the tested specimen, and RAV is the clockwise rotation angle of the sensor with the initial position as the origin and the tested specimen as the center.

3.2. Experimental Procedures and Data Acquisition Method

In this study, the experimental phenomena were described by the applied tension, which could be converted into stresses in the relevant results. The test specimens were

pulled up at a constant speed of 2 kN/s using the universal testing machine, with the loading range varying from 0 to 160 kN. At every 10 kN increase in tension, the machine paused to maintain the current load. This process was repeated for a total of 17 loading levels. The SMFL signals were collected by the sensor at the middle section of the specimen, specifically from 25 cm to 55 cm (y = 0~30 cm). Data were collected at every 1 cm interval, resulting in 31 sampling points. After completing the scan under the current load, the machine was loaded to the next level, and the scanning process continued.

To investigate the spatial SMFL field distribution of steel strands under different tension levels, a graded loading test was designed using three Lift-Off Values (LOV) (H_1 = 0.5 cm, H_2 = 1.5 cm, H_3 = 3 cm) and three Rotation Angle Values (RAV) (θ_1 = 0°, θ_2 = 120°, θ_3 = 240°). Sensors were used to scan the SMFL field on the surface of the specimen at a total of 9 detection positions within the range of y = 0~30 cm. Refer to Table 2 and Figure 3 for specific details.

Table 2. Arrangement of detection positions.

	θ_1 = 0°	θ_2 = 120°	θ_3 = 240°
H_1 = 0.5 cm	P_1	P_2	P_3
H_2 = 1.5 cm	P_4	P_5	P_6
H_3 = 3 cm	P_7	P_8	P_9

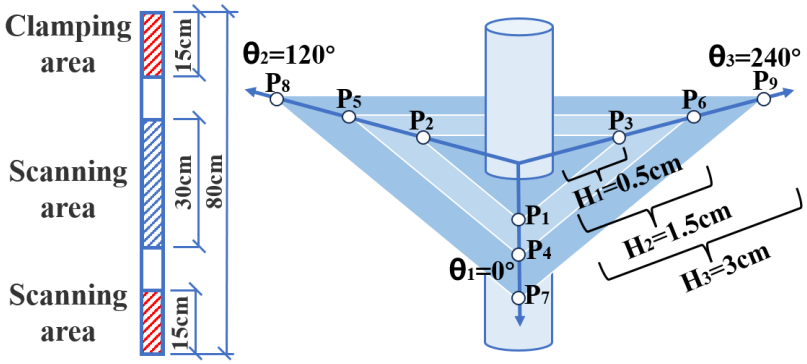

Figure 3. Schematic diagram of the detection area and detection positions.

4. Experimental Results

The SMFL field is a weak magnetic field, resulting in lower flux density in the measured signals. At the same detection location, we measured the leakage magnetic field in the presence and absence of the specimen, referred to as the scanning and external fields, respectively. As discussed in Section 2, ferromagnetic materials generate an additional magnetic field on their surface when subjected to applied stress. This phenomenon means that the scanning magnetic field consists of the external and SMFL fields under tension. The SMFL field discussed in this manuscript is obtained by subtracting the external field from the scanning field. This process is considered as shielding against the Earth's magnetic field and other steel objects' proximity, effectively eliminating a significant amount of noise.

4.1. Magnetic Scanning Curve Distribution

The distribution of the scanning magnetic field at detection position P_1 (H_1 = 0.5 cm, θ_1 = 0°) is illustrated in Figure 4, where By represents the tangential component of the magnetic field, Bz represents the normal component of the magnetic field, and Bx represents the magnetic field component perpendicular to the B*y*–Bz plane. The distribution patterns of the scanning magnetic field are as follows:

(1) The Bx curve gradually increased along the scanning path, with a significantly lower rate of change in the middle region (y = 10 cm~20 cm) compared to the two ends. As the tension in the specimen changed, the Bx curve shifted as a whole, with similar

trends and a relatively high degree of coincidence. In the y = 0~16 cm region, the Bx curves corresponding to F = 80 kN and F = 60 kN were located above and below the overall curve, respectively;

(2) The By curve showed a quadratic-like shape, decreasing first and then increasing along the scanning path, reaching the minimum value at y = 14cm. Similar to the Bx curve, the rate of change of the By curve in the middle region was lower than at the two ends. The shape of the By curve remained similar with varying applied stress, and the magnetic field curves intersected at y = 3 cm and y = 28 cm for different tension levels;

(3) The Bz curve followed a cubic-like shape, with significant differences in the magnetic field curves under different tension levels. When F = 0 kN, the Bz curve first increased, then decreased, and finally increased again along the scanning path. There were two distinct peaks at y = 8 cm and y = 25 cm, and as the tension in the steel strand increased, these peaks gradually flattened. Similar to the other two components, the Bz curve also showed a lower rate of change in the middle region compared to the two ends.

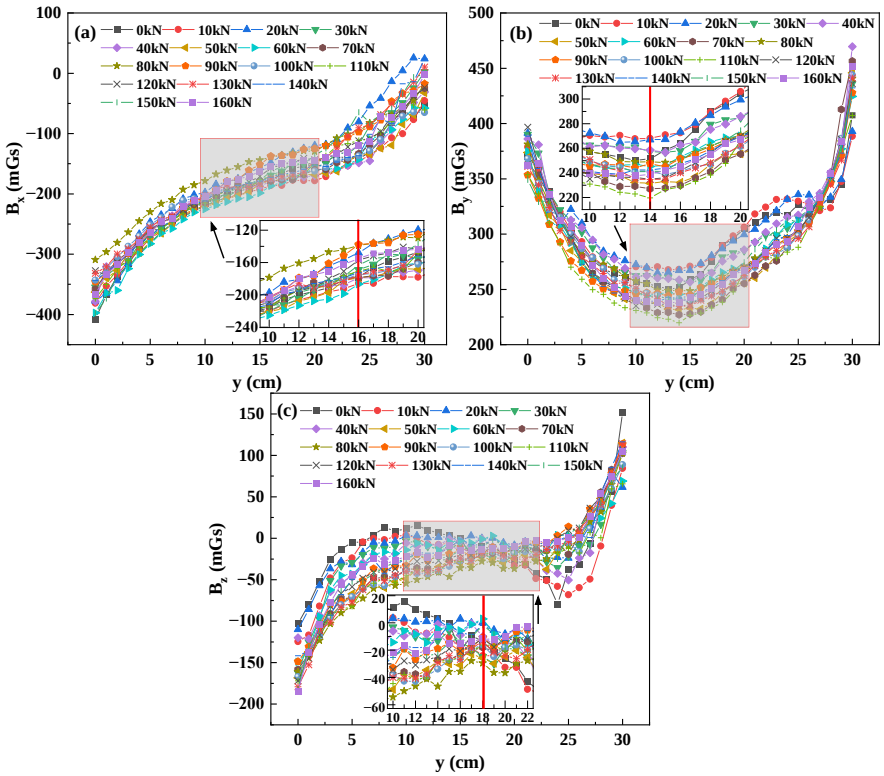

Figure 4. Scanning magnetic field distribution at P_1. (**a**) Bx component of Scanning magnetic field; (**b**) By component of Scanning magnetic field; (**c**) Bz component of Scanning magnetic field.

4.2. SMFL Field Curve Distribution

The distribution of the external magnetic field at detection position P_1 is depicted in Figure 5a. By subtracting the external magnetic field from the scanning magnetic field discussed in Section 4.1, the SMFL field of the specimen was obtained, as shown in Figure 5b–d. The distribution patterns of the SMFL field were as follows:

(1) The Bx curve decreased along the scanning path. When y < 15 cm, the curves for different loads were approximately parallel and linearly declined. The curve bulged upward between y = 15 cm and 26 cm, and some curves intersected. When y > 26 cm, the curves exhibit severe fluctuations, and at y = 30 cm, the curve showed a significant drop, reaching the minimum value;

(2) The By curve exhibited drastic changes at both ends of the scanning region and remained relatively flat in the middle area (y = 10 cm~20 cm). When y < 11 cm, the curve showed a significant upward trend along the scanning path, and the curves for different loads were approximately parallel. Between y = 11 cm to 27 cm, the curve's variation was relatively small, with the most significant change of 39.1 mGs for the 0 kN curve. When y > 27 cm, the curves converged and increased dramatically, reaching the maximum value at y = 30 cm;

(3) The Bz curve was similar to the By curve, with more significant changes at the ends than in the middle region. When y < 6 cm, the curves rapidly decreased and were relatively close to each other. Between y = 6 cm to 20 cm, the curves entered the "gentle region" with more minor variations than the previous region. The magnitude of the curve changes decreased further with increasing load, causing the distance between different curves to first increase, then fall, and finally intersect at y = 20 cm. When y > 20 cm, the distance between the curves increased again, and the curve's trend changed around y = 25 cm.

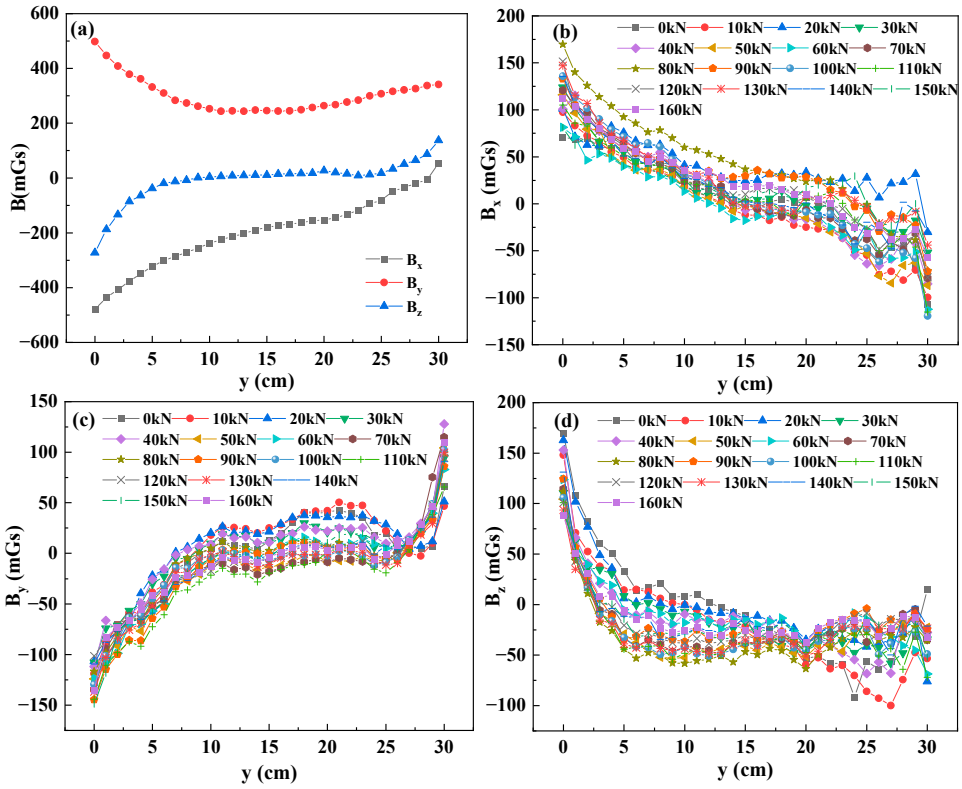

Figure 5. Distribution curves of external magnetic field and SMFL field at P_1. (**a**) External magnetic field; (**b**) Bx component of SMFL field; (**c**) By component of SMFL field; (**d**) Bz component of SMFL field.

Upon analyzing the scanning magnetic field and SMFL field curves, it was evident that the three components of the two magnetic fields differ significantly in magnitude and shape. However, they shared a common characteristic of exhibiting a lower rate of change in the middle region compared to the two ends. This phenomenon could be attributed to the influence of the fixture's magnetic field in the areas near the ends. The curves for different loads tended to converge and become nearly parallel at the ends, while they dispersed in the middle region. However, the curves of the other components, besides the tangential component Bx, exhibited clear intersection points. This phenomenon could be attributed to transforming the internal magnetic domains from a random distribution to an oriented distribution under increasing load, resulting in regular changes on the specimen's surface.

Compared to the other two components, the normal component Bz of the scanning magnetic field and leakage magnetic field had two distinct intersection points at y = 18 cm and 20 cm, respectively. These curves showed different features and exhibited regular changes under stress. Thus, further analysis of the normal component Bz of the SMFL field is necessary in the next section. The effect of load on the SMFL field intensity at various sampling points on the Bz curve was discussed, and the distribution of the spatial SMFL field under load was analyzed. A magnetic feature parameter was proposed to characterize the stress state of the steel strand, resulting in a stress measurement method based on the spatial SMFL distribution.

5. Discussion

5.1. Influence of Load on SMFL Intensity at Each Sampling Point

To investigate the stress characterization method for steel strands based on magnetic feature parameters, it was necessary to explore the influence of loads on the SMFL field at various sampling points. The relationship between the leakage magnetic field and the applied loads is shown in Figure 6. The 31 curves in the graph represent the 31 sampling points along the scanning path, and the horizontal axis represents the loads applied on the specimen (0~160 kN).

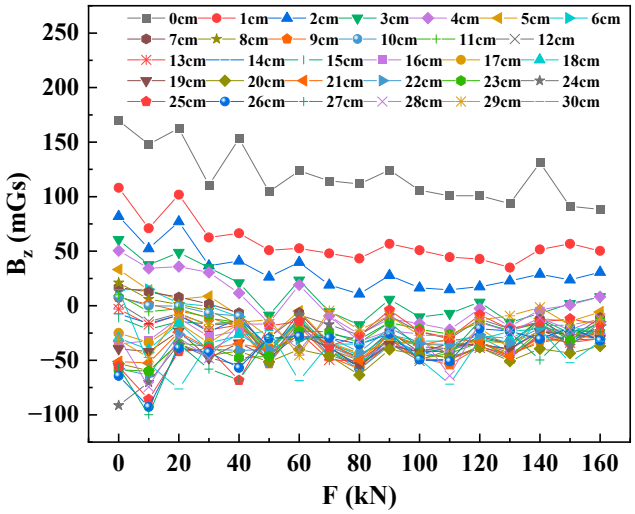

Figure 6. Magnetic force curves of each sampling point on the scanning path.

During the loading process, there were significant variations in the magnetic field intensity at different positions. The magnetic force curves for the sampling points near the ends (such as points 1–5 and 26–30) exhibited more significant fluctuations and were located on the outer side of all curves, far from other curves. This observation was consistent with the inference mentioned in Section 4.1 that the fixture influenced magnetic fields more at the ends.

When F was 0~50 kN, the Bz curve changed rapidly and showed an overall downward trend. When F exceeded 50 kN, the Bx values fluctuated within a small range. The range from F = 0 to 50 kN was referred to as Region 1; the remaining range was Region 2. There were distinct differences in the curve distributions between these two regions. The range of data in Region 1 (R_1) was generally more extensive than in Region 2 (R_2), and their difference was calculated as $\Delta = R_1 - R_2$. The results are shown in Figure 7.

It can be observed that, except at points y = 16 cm and 29 cm, the range of data in Region 1 was generally greater than that in Region 2 ($\Delta > 0$) within the scope of y = 14~20 cm. Moreover, the range values within this range were relatively small, indicating that the values vary within a narrow range.

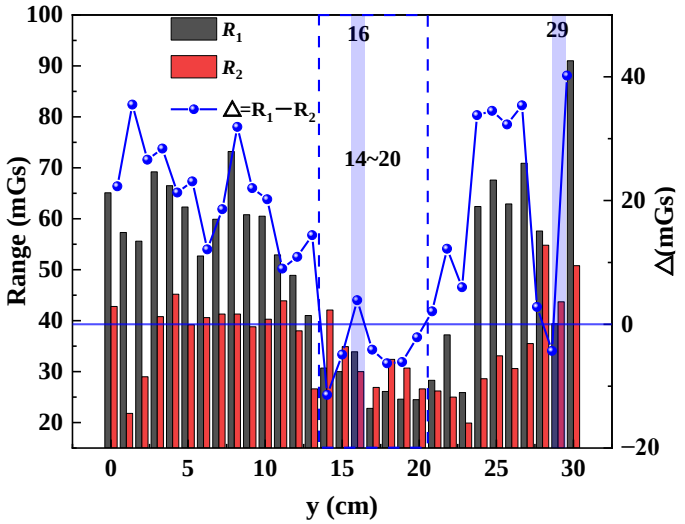

Figure 7. The range of data in Region 1 and Region 2.

5.2. Influence of Load on the Spatial SMFL Distribution

Based on the analysis conducted in Sections 3.1 and 5.1, it was evident that under axial loading, the magnetic force curves at different sampling points on the steel strand exhibited significant variations in numerical values and diverse patterns of change. Such a phenomenon made identifying stress concentration points difficult. Evaluating the stress on the specimen directly based on the SMFL intensity or extreme values and differences in the magnetic force curves from a single sampling point was also challenging. Therefore, it was necessary to extract SMFL curve characteristics to characterize the stress state of the specimen effectively.

Regarding the normal component of the leakage magnetic field (Bz), when the load was small (e.g., F = 0 kN), its corresponding curve rapidly decreased along the scanning path and started to rise after y > 25 cm. As the load increased, a "gentle zone" appeared in the SMFL curve, where the change was significantly smaller than in the first and last areas. When the load was large (e.g., F = 160 kN), its corresponding curve only dropped rapidly at y < 6 cm and the subsequent curve exhibited slight fluctuations within a specific range.

Based on the above analysis, it was observed that as the applied load on the specimen increased, the variation in the normal component of the SMFL field (Bz) became gentler, with reduced slope, range, and fluctuation. It was necessary to identify a parameter that could evaluate the scope and fluctuation of the data. AVEDEV is a function commonly used to assess data dispersion and is denoted here as *A*. The formula for calculating AVEDEV for the Bz curve of the leakage magnetic field component is given by Equation (11):

$$Avedev = \frac{1}{n-1}\sum_{i=1}^{n-1}|B_{z_{i+1}} - \overline{B_z}| \tag{11}$$

In this experiment, the parameter *A* for each load level curve was calculated using Equation (11), resulting in the A–F curves for each of the nine detection positions. Each curve contained 17 data points, representing a 17-level load, as shown in Figure 8. This figure provided preliminary insight into the correspondence between the SMFL signals and the applied load on the specimen.

From Figure 8, it is evident that *A* decreased monotonically with the increase in load F, indicating that the dispersion of the Bz curve reduced as the tensile force on the specimen increased. However, there were significant differences in the distribution of A–F curves for different detection positions. For example, the curves for P_3 and P_6 had larger ranges and more extreme values than others. In contrast, the curves for P_1, P_5, and P_8 exhibited a more pronounced change in range in Region 1 compared to Region 2, and the other curves showed relatively uniform changes, presenting an excellent linear relationship.

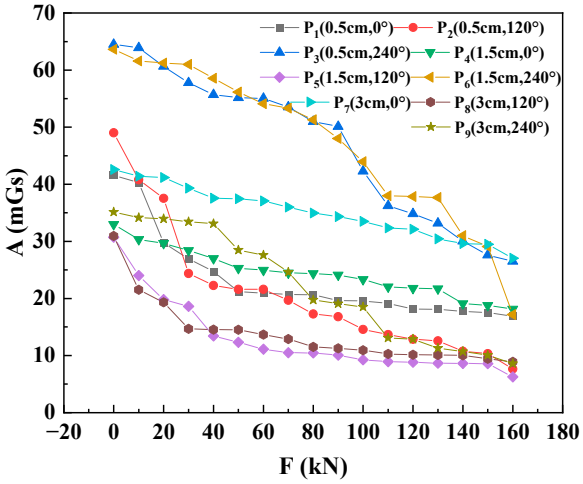

Figure 8. A–F curve of leakage magnetic field direction component Bz.

To achieve stress measurement based on the spatial SMFL field distribution in the steel strand, it was necessary to understand how the spatial detection positions influence the distributions of A–F curves. These positions were determined by two factors: the LOV and the RAV. The curves corresponding to the same factors were plotted together in Figures 9 and 10.

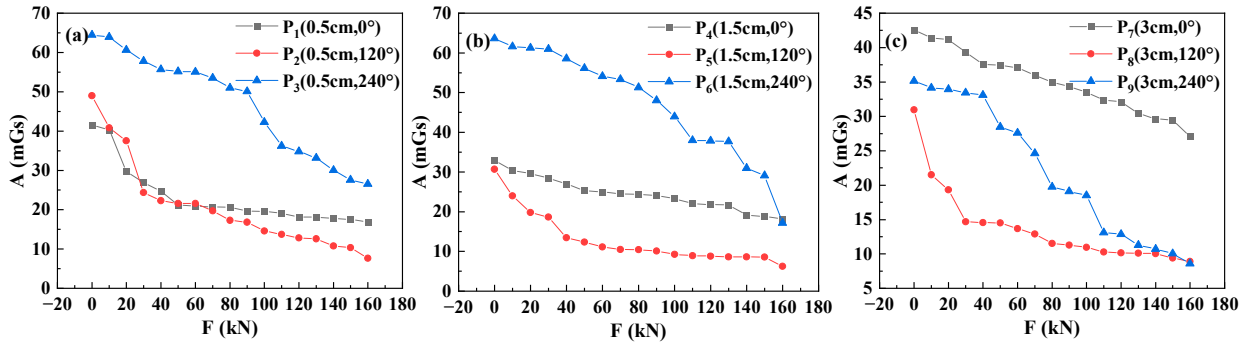

Figure 9. A–F curves of the same LOV: (**a**) H_1 = 0.5 cm; (**b**) H_2 = 1.5 cm; (**c**) H_3 = 3 cm.

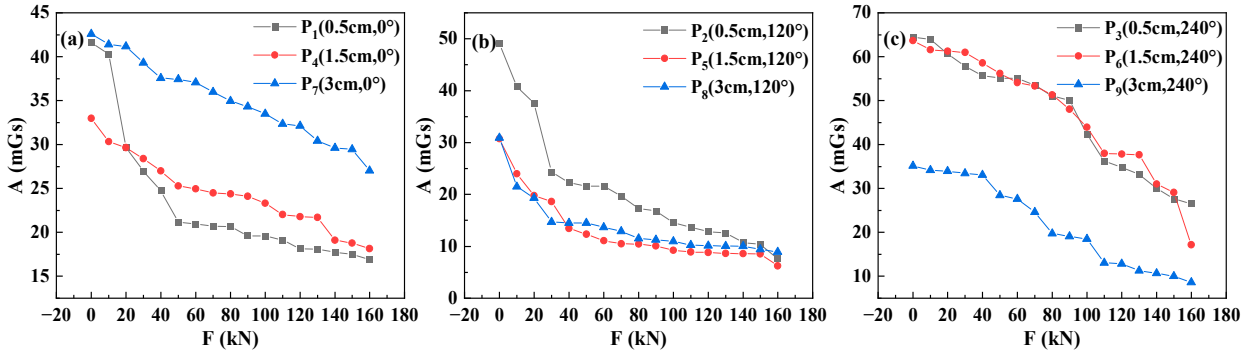

Figure 10. A–F curves with the same RAV: (**a**) $\theta_1 = 0°$; (**b**) $\theta_2 = 120°$; (**c**) $\theta_3 = 240°$.

From Figures 9 and 10, it can be observed that the RAV affected both the range and rate of change of the A–F curves, while the LOV mainly influenced the numerical values of the curves, with minimal impact on their shape. Except when H_1 = 0.5 cm, the range of the curves for $\theta_3 = 240°$ was smaller than $\theta_2 = 120°$, the range of the curves decreased in the order of θ_3, θ_2, and θ_1, and any parameter A for θ_2 was smaller than those for θ_3 and θ_1. Moreover, with an increase in load value, the rate of change for the A–F curves

corresponding to $\theta_1 = 0°$ and $\theta_3 = 240°$ did not exhibit significant differences. In contrast, the rate of change for the curve corresponding to $\theta_2 = 120°$ gradually decreased.

Based on the above analysis, it is evident that as the tensile force on the specimen increases, the dispersion of the SMFL curves decreases. The RAV affected the range and rate of change of the dispersion, while the LOV influenced the numerical values. To achieve stress measurement based on the spatial SMFL fields in the steel strand, it was necessary to establish a relationship between parameter A and the applied external load. However, due to significant differences in the range of A–F curves for different detection positions, the further processing of parameter A was needed.

5.3. Stress Characterization Method of Steel Strand Based on Magnetic Characteristic Parameter

To better quantify the dispersion of the Bz curve, the parameter A was normalized to obtain A_N through Equation (12).

$$A_N = \frac{A_i - A_{min}}{A_{max} - A_{min}} \tag{12}$$

Figure 11 shows that the A_N values decreased with the increase in F after normalization, and an excellent linear relationship between A_N and F was observed. Some A_N–F curves exhibit a concave trend, indicating that the dispersion changes more rapidly in the early loading stage compared to the later stage. This phenomenon was attributed to the transition of scattered magnetic domains to a more regular distribution during the initial loading, significantly affecting the magnetic field distribution. As the loading progresses, the magnetic domains tend to have a more regular distribution, leading to a gradual reduction in their influence on the variation of the SMFL field.

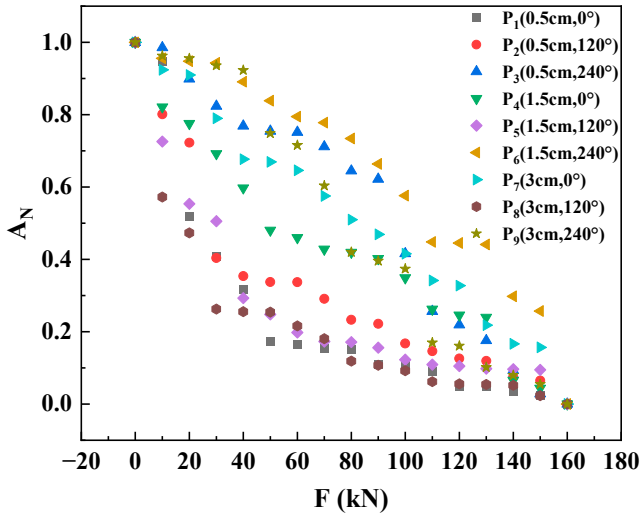

Figure 11. Normalized result of parameter A.

A linear fitting was performed on the A_N–F data to establish the correspondence between A_N and F, as shown in Figure 9. The fitting results are summarized in Figure 12 and Table 3.

Table 3. Linear fitting results of A_N–F curve of each detection position.

		$\theta_1 = 0°$		$\theta_2 = 120°$		$\theta_3 = 240°$
H_1 = 0.5 cm	P_1	y = −0.00506x + 0.6576 R^2 = 0.7016	P_2	y = −0.00499x + 0.7168 R^2 = 0.8179	P_3	y = −0.00667x + 1.0721 R^2 = 0.9594
H_2 = 1.5 cm	P_4	y = −0.00546x + 0.8652 R^2 = 0.9574	P_5	y = −0.00454x + 0.6369 R^2 = 0.7304	P_6	y = −0.00559x + 1.095 R^2 = 0.9364
H_3 = 3 cm	P_7	y = −0.00589x + 0.9809 R^2 = 0.9887	P_8	y = −0.00419x + 0.5579 R^2 = 0.6923	P_9	y = −0.00722x + 1.0834 R^2 = 0.9668

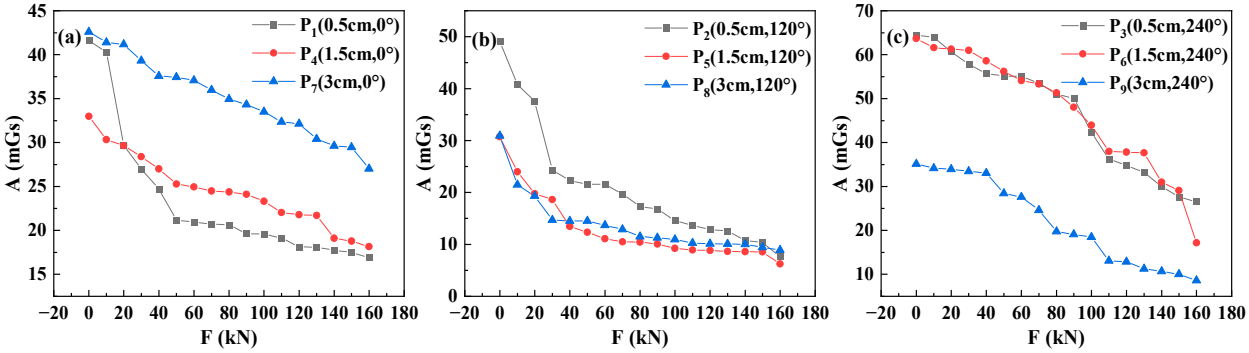

Figure 12. Linear fitting result of A_N–F curve with the same LOV: (**a**) H_1 = 0.5 cm; (**b**) H_2 = 1.5 cm; (**c**) H_3 = 3 cm.

The linear fitting curve formula is:

$$A_N = K \cdot F + B \tag{13}$$

The formula for calculating the stress of the specimen can be obtained from this:

$$\sigma = \frac{F}{S} = \frac{A_N - B}{K \cdot S} \tag{14}$$

where S is the cross-sectional area of the specimen, and the values of K and B were as follows:

From Table 4, it can be observed that the values for K and B changed depending on the detection position. At $\theta_1 = 0°$, the absolute values of K and B increased with LOV (H). At $\theta_2 = 120°$, K and B's absolute values decreased as H increases. At $\theta_3 = 240°$, the relationship between the absolute values of K, B, and H was more complicated. That is why choosing the appropriate parameters based on the detection position was essential when calculating the specimen's stress using Equation (14).

Table 4. The values of the parameters K and B at each detection position.

		$\theta_1 = 0°$			$\theta_2 = 120°$			$\theta_3 = 240°$	
		K	***B***		***K***	***B***		***K***	***B***
H_1 = 0.5 cm	P_1	−0.00506	0.6576	P_2	−0.00499	0.7168	P_3	−0.00667	1.0721
H_2 = 1.5 cm	P_4	−0.00546	0.8652	P_5	−0.00454	0.6369	P_6	−0.00559	1.095
H_2 = 1.5 cm	P_7	−0.00589	0.9809	P_8	−0.00419	0.5579	P_9	−0.00722	1.0834

Figures 12 and 13 and Table 4 show that the linear fitting results of A_N–F curves for different detection positions exhibited significant differences, and both the LOV and RAV can influence the fitting results. At $\theta_1 = 0°$, the fitting function's linear correlation coefficient (R^2) increased with the increasing H, and all LOVs except H_1 = 0.5 had an R^2 greater than 0.95, which means good linearity. At $\theta_2 = 120°$, the R^2 decreased with increased H and was less than 0.82, indicating poor linearity. At $\theta_3 = 240°$, the R^2 only slightly changed with H and was always greater than 0.93, indicating good linearity.

Based on the above analysis, it can be concluded that the dispersion of the normal component of the SMFL field in the steel strand decreased as the stress on the specimen increased. The degree of dispersion A was normalized for each detection position as a feature of value $A_{N,}$ and linear regression was performed to establish a relationship between the distribution of the SMFL field and the stress on the specimen. The results indicate that the LOV and RAV could influence the final fitting curves. Among the three rotation angle values, $\theta_3 = 240°$ exhibited the best linearity and stability in the fitting results, while $\theta_2 = 120°$ showed the worst linearity, with $\theta_1 = 0°$ lying in between them.

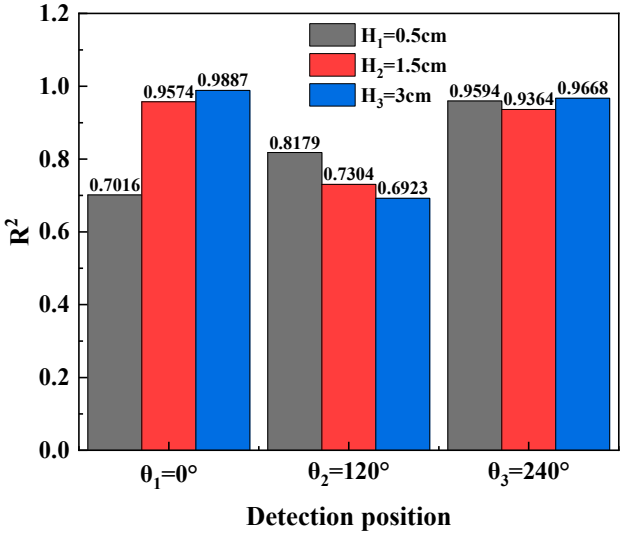

Figure 13. Linear fitting correlation coefficient of each detection position.

6. Conclusions

This study aimed to develop a stress measurement method for steel strands based on the spatial distribution of the SMFL field. A graded loading test for steel strands was designed to achieve this, and nine detection positions with different LOV and RAV were set to detect the spatial SMFL field. The original magnetic field and SMFL field distribution on the specimen surface under graded loading, the numerical values, the range of variation, and the curve shape of the normal component of the leakage magnetic field (Bz) were discussed. The study proposed a stress calculation method for steel strands based on the magnetic characteristic parameter A_N and investigated the influence of LOV and RAV on the detection results. The following conclusions were drawn:

(1) External magnetic fields and fixture-induced magnetic fields significantly impact the distribution of the SMFL field. Regardless of whether the influence of the external magnetic field was excluded, the curves of all components of the SMFL field exhibited a "three-segment" pattern, with drastic changes at the beginning (Y = 0~5 cm) and end (Y = 25~30 cm) of the curves and relatively smooth changes in the middle;

(2) When the external load was in the range of F = 0~50 kN, the variation range of the SMFL field intensity at the sampling points was greater than in the subsequent loading stages. There were noticeable differences in the SMFL field intensity values at different sampling points along the same scanning path during loading. However, there was no clear correspondence between the SMFL field intensity and the stress level of the specimen. Consequently, evaluating the stress level of the specimen solely based on the SMFL field intensity from a single detection point proved challenging;

(3) As the external load increased, the dispersion of the normal component of the SMFL field curve (Bz) on the surface of the steel strand decreased gradually. The magnetic characteristic parameter A_N could be used to evaluate the dispersion of the Bz curve, and there was a good linear relationship between A_N and F. By performing linear fitting, a formula for calculating the stress of the steel strand based on the magnetic characteristic parameter A_N was obtained;

(4) The LOV and RAV significantly affected the results of the linear fitting, and the specific detection positions determined the parameters of the stress calculation formula. Therefore, it is essential to conduct experiments at multiple spatial locations to optimize the formula parameters in the future.

Author Contributions: Conceptualization, S.L. and C.C.; methodology, S.L. and R.Z.; software, S.L.; validation, R.Z., J.Z. and K.T.; formal analysis, S.L.; investigation, J.Z.; resources, R.Z.; data curation, C.C.; writing—original draft preparation, S.L.; writing—review and editing, S.L.; visualization, S.L.;

supervision, K.T.; project administration, J.Z.; funding acquisition, C.C. All authors have read and agreed to the published version of the manuscript.

Funding: This work was supported by the National Natural Science Foundation of China (U20A20314), the Chongqing Natural Science Foundation of China (CSTB2022NSCQ-LZX0006, cstc2022ycjh-bgzxm0086), and Major Scientific Research Projects of China Railway Group Co., Ltd. (2022-ZD-11).

Data Availability Statement: The data presented in this study are available from the first and corresponding author upon request. The data are not publicly available due to the policy of the data provider.

Conflicts of Interest: The authors declare no conflict of interest.

References

1. Minaei, A.; Daneshjoo, F.; Goicolea, J.M. Experimental and numerical study on cable breakage equivalent force in cable-stayed structures consisting of low-relaxation seven-wire steel strands. *Structures* **2020**, *27*, 595–606. [CrossRef]
2. Zhang, Y.; Fang, Z.; Jiang, R.; Xiang, Y.; Long, H.; Lu, J. Static Performance of a Long-Span Concrete Cable-Stayed Bridge Subjected to Multiple-Cable Loss during Construction. *J. Bridge Eng.* **2020**, *25*, 04020002.1–04020002.16. [CrossRef]
3. Xin, J.; Zhou, C.; Jiang, Y.; Tang, Q.; Yang, X.; Zhou, J. A signal recovery method for bridge monitoring system using TVFEMD and encoder-decoder aided LSTM. *Measurement* **2023**, *214*, 112797. [CrossRef]
4. Yang, J.; Chen, R.; Zhang, Z.; Zou, Y.; Zhou, J.; Xia, J. Experimental study on the ultimate bearing capacity of damaged RC arches strengthened with ultra-high performance concrete. *Eng. Struct.* **2023**, *279*, 115611. [CrossRef]
5. Yao, Y.; Yan, M.; Bao, Y. Measurement of cable forces for automated monitoring of engineering structures using fiber optic sensors: A review. *Autom. Constr.* **2021**, *126*, 103687. [CrossRef]
6. Fu, Z.; Ji, B.; Wang, Q.; Wang, Y. Cable force calculation using vibration frequency methods based on cable geometric parameters. *J. Perform. Constr. Facil.* **2017**, *31*, 04017021. [CrossRef]
7. Ni, Y.; Zhang, Q.; Xin, R. Magnetic flux detection and identification of bridge cable metal area loss damage. *Measurement* **2021**, *167*, 108443. [CrossRef]
8. Zhang, L.; Qiu, G.; Chen, Z. Structural health monitoring methods of cables in cable-stayed bridge: A review. *Measurement* **2021**, *168*, 108343. [CrossRef]
9. Wang, Z.D.; Yao, K.; Deng, B.; Ding, K.Q. Quantitative study of metal magnetic memory signal versus local stress concentration. *NDT E Int.* **2010**, *43*, 513–518. [CrossRef]
10. Dubov, A.A. A study of metal properties using the method of magnetic memory. *Met. Sci. Heat Treat.* **1997**, *39*, 401–405. [CrossRef]
11. Wang, Z.D.; Yao, K.; Deng, B.; Ding, K.Q. Theoretical studies of metal magnetic memory technique on magnetic flux leakage signals. *NDT E Int.* **2010**, *43*, 354–359. [CrossRef]
12. Shi, P.; Su, S.; Chen, Z. Overview of researches on the nondestructive testing method of metal magnetic memory: Status and challenges. *J. Nondestruct. Eval.* **2020**, *39*, 43. [CrossRef]
13. Liu, B.; Fu, Y.; Xu, B. Study on metal magnetic memory testing mechanism. *Res. Nondestruct. Eval.* **2015**, *26*, 1–12. [CrossRef]
14. Wang, Z.D.; Gu, Y.; Wang, Y.S. A review of three magnetic NDT technologies. *J. Magn. Magn. Mater.* **2012**, *324*, 382–388. [CrossRef]
15. Bao, S.; Jin, P.; Zhao, Z.; Fu, M. A review of the metal magnetic memory method. *J. Nondestruct. Eval.* **2020**, *39*, 11. [CrossRef]
16. Pospisil, K.; Manychova, M.; Stryk, J.; Korenska, M.; Matula, R.; Svoboda, V. Diagnostics of reinforcement conditions in concrete structures by GPR, impact-echo method and metal magnetic memory method. *Remote Sens.* **2021**, *13*, 952. [CrossRef]
17. Dubov, A.; Dubov, A.; Kolokolnikov, S. Application of the metal magnetic memory method for detection of defects at the initial stage of their development for prevention of failures of power engineering welded steel structures and steam turbine parts. *Weld. World* **2014**, *58*, 225–236. [CrossRef]
18. Shi, M.; Liang, Y.; Zhang, M.; Huang, Z.; Feng, L.; Zhou, Z. Pipeline damage detection based on metal magnetic memory. *IEEE Trans. Magn.* **2021**, *57*, 1–15. [CrossRef]
19. Zhao, B.; Yao, K.; Wu, L.; Li, X.; Wang, Y.S. Application of metal magnetic memory testing technology to the detection of stress corrosion defect. *Appl. Sci.* **2020**, *10*, 7083. [CrossRef]
20. Shi, P. Magneto-mechanical model of ferromagnetic material under a constant weak magnetic field via analytical anhysteresis solution. *J. Appl. Phys.* **2020**, *128*, 115102. [CrossRef]
21. Yang, X.; He, C.; Pu, H.; Chen, L. An extended magnetic-stress coupling model of ferromagnetic materials based on energy conservation law and its application in metal magnetic memory technique. *J. Magn. Magn. Mater.* **2022**, *544*, 168653. [CrossRef]
22. Xia, R.; Zhou, J.; Zhang, H.; Zhou, D.; Zhang, Z. Experimental study on corrosion of unstressed steel strand based on metal magnetic memory. *KSCE J. Civ. Eng.* **2019**, *23*, 1320–1329. [CrossRef]
23. Pang, C.; Zhou, J.; Zhao, R.; Ma, H.; Zhou, Y. Research on internal force detection method of steel bar in elastic and yielding stage based on metal magnetic memory. *Materials* **2019**, *12*, 1167. [CrossRef] [PubMed]
24. Zhao, X.; Su, S.; Wang, W.; Zhang, X. Metal magnetic memory inspection of Q345B steel beam in four point bending fatigue test. *J. Magn. Magn. Mater.* **2020**, *514*, 167155. [CrossRef]

25. Liu, B.; Zeng, Z.; Wang, H. Study on the early fatigue damage evaluation of high strength steel by using three components of metal magnetic memory signal. *NDT E Int.* **2021**, *117*, 102380. [CrossRef]
26. Roskosz, M. Metal magnetic memory testing of welded joints of ferritic and austenitic steels. *NDT E Int.* **2011**, *44*, 305–310. [CrossRef]
27. Roskosz, M.; Gawrilenko, P. Analysis of changes in residual magnetic field in loaded notched samples. *NDT E Int.* **2008**, *41*, 570–576. [CrossRef]
28. Roskosz, M.; Bieniek, M. Analysis of the universality of the residual stress evaluation method based on residual magnetic field measurements. *NDT E Int.* **2013**, *54*, 63–68. [CrossRef]
29. Zhou, J.; Qiu, J.; Zhou, Y.; Zhou, Y.; Xia, R. Experimental study on residual bending strength of corroded reinforced concrete beam based on micromagnetic sensor. *Sensors* **2018**, *18*, 2635. [CrossRef]
30. Huang, H.; Jiang, S.; Yang, C.; Liu, Z. Stress concentration impact on the magnetic memory signal of ferromagnetic structural steel. *Nondestruct. Test. Eval.* **2014**, *29*, 377–390. [CrossRef]
31. Yao, K.; Deng, B.; Wang, Z.D. Numerical studies to signal characteristics with the metal magnetic memory-effect in plastically deformed samples. *NDT E Int.* **2012**, *47*, 7–17. [CrossRef]
32. Zhang, H.; Li, H.; Zhou, J.; Tong, K.; Xia, R. A multi-dimensional evaluation of wire breakage in bridge cable based on self-magnetic flux leakage signals. *J. Magn. Magn. Mater.* **2023**, *566*, 170321. [CrossRef]
33. Wang, H.; Dong, L.; Wang, H.; Ma, G.; Xu, B.; Zhao, Y. Effect of tensile stress on metal magnetic memory signals during on-line measurement in ferromagnetic steel. *NDT E Int.* **2021**, *117*, 102378. [CrossRef]
34. Leng, J.; Liu, Y.; Zhou, G.; Gao, Y. Metal magnetic memory signal response to plastic deformation of low carbon steel. *NDT E Int.* **2013**, *55*, 42–46. [CrossRef]
35. Ren, S.; Ren, X. Studies on laws of stress-magnetization based on magnetic memory testing technique. *J. Magn. Magn. Mater.* **2018**, *449*, 165–171. [CrossRef]
36. Tong, K.; Zhang, H.; Zhao, R.; Zhou, J.; Ying, H. Investigation of SMFL monitoring technique for evaluating the load-bearing capacity of RC bridges. *Eng. Struct.* **2023**, *293*, 116667. [CrossRef]
37. Qu, Y.; Zhang, H.; Zhao, R.; Liao, L.; Zhou, Y. Research on the method of predicting corrosion width of cables based on the spontaneous magnetic flux leakage. *Materials* **2019**, *12*, 2154. [CrossRef]
38. Liu, S.; Sun, Y.; Jiang, X.; Kang, Y. Comparison and analysis of multiple signal processing methods in steel wire rope defect detection by hall sensor. *Measurement* **2021**, *171*, 108768. [CrossRef]
39. Jiles, D.C. Theory of the magnetomechanical effect. *J. Phys. D Appl. Phys.* **1995**, *28*, 1537. [CrossRef]
40. Jiles, D.C.; Atherton, D.L. Theory of ferromagnetic hysteresis. *J. Magn. Magn. Mater.* **1986**, *61*, 48–60. [CrossRef]
41. Li, J.; Xu, M. Modified Jiles-Atherton-Sablik model for asymmetry in magnetomechanical effect under tensile and compressive stress. *J. Appl. Phys.* **2011**, *110*, 8. [CrossRef]
42. Li, J.; Xu, M.; Leng, J.; Xu, M. Modeling plastic deformation effect on magnetization in ferromagnetic materials. *J. Appl. Phys.* **2012**, *111*, 1. [CrossRef]